

Formation of hydrothermal corrugations during weathering of ultramafic rocks

Formation de corrugations hydrothermales lors de l'altération des roches ultramafiques

Laurent Guillou-Frottier⁽¹⁾, Anicet Beauvais⁽²⁾, Robert Wyls⁽¹⁾,
Laurent Bailly⁽¹⁾, Thierry Augé⁽¹⁾, Anne-Sophie Audion^(1,3)

(1) BRGM, ISTO, UMR 7327, 3 av. C. Guillemin, BP 36009, 45060 Orléans Cedex 2, France

(2) Aix-Marseille University, CEREGE (IRD, CNRS), Aix-en-Provence, France

(3) Now at Variscan Mines, Orléans, France

l.guillou-frottier@brgm.fr

I. INTRODUCTION

The chemical weathering reactions of ferro-magnesian minerals (biotite, pyroxenes, olivine) may involve a volume expansion that results in stress-induced fracture networks, increasing the permeability and porosity (Wyls et al., 2004; Royne et al., 2008; Lachassagne et al., 2011). In addition, hydration reactions are also highly exothermic so that local temperatures may exceed several tens of °C (McDonald and Fyfe, 1985; Kelemen and Hirth, 2012). When combined together, the reaction-induced fracturing and reaction-induced heating may trigger thermal convection. In the case of ultramafic rocks, olivine hydration is highly exothermic and causes important permeability changes (Plümper et al., 2012). Fluid flow regimes in porous media are often described as being controlled by gravity and pressure gradients (topography-driven flow). Here, we investigate the possibility of an additional fluid flow regime (buoyancy-driven flow), which would be triggered by high temperatures resulting from exothermic weathering reactions in ultramafic rocks.

During deepening of the weathering front at a velocity of a few m Myr⁻¹ over several tens of Myr (Vasconcelos and Conroy, 2003) the weathered medium may have experienced continuous heating by hydration reactions. Our goal is thus to assess the likelihood of convective flow in a medium where permeability and heat production values are not only anomalously high, but also depth- and time-dependent. Our study focuses on the weathered ultramafic rocks of New Caledonia, where some puzzling questions and observations remain, such as the undulated lithological interfaces, including the weathering front itself, which shows three-dimensional corrugations (or "egg-box topography").

II. ANOMALOUSLY HOT TEMPERATURES AT SHALLOW DEPTHS

In the ophiolitic belt of Oman, current alteration of ultramafic rocks via serpentinization reactions leads to the formation of many hyperalkaline warm springs whose temperatures reach 41 °C (Dewandel et al., 2005; Chavagnac et al., 2013). In the California Coast Range, the ¹⁸O/¹⁶O fractionation between serpentine and magnetite indicate a temperature of lizardite-chrysotile serpentinization ranging from 85 to 115 °C (Wenner and Taylor, 1971), that suggests a probable exothermic reaction between ultramafic rocks and meteoric groundwater.

In New Caledonia, alkaline springs of the Prony area (south end of the Island) discharge waters at temperatures up to 42 °C at the Carénage spring (Launay and Fontes, 1985). The waters of the neighboring Dumbea and Kaoris Rivers altered the peridotite bedrock to serpentine and have temperatures ranging from 23 °C to 34 °C (Barnes et al., 1978). In addition, the isotopic signatures of "garnierite" (the local name for nickel-bearing phyllosilicates) occurrences also indicate formation temperatures much higher than present-day ground surface temperatures (Amisse et al., 2010). Analyses of quartz-talc couples indicate that mineral precipitation occurred around 50 °C. Another recent study on magnesite veins from the

serpentine sole of the Koniambo massif indicate that fluids were in equilibrium with their host rocks at temperatures of 38 to 77 °C (Quesnel et al., 2013).

Although temperature was not directly measured in lateritic profiles of New Caledonia, the need for such present-day evidence of hot fluids at shallow depths is not necessarily required since fluid flow regimes probably show transient features in a system whose geometry is time-dependent. Evidence of possible hot temperatures in the past is sufficiently puzzling to investigate the likelihood of previous convective flow in lateritic weathering mantles.

III. PECULIARITIES OF ULTRAMAFIC LATERITES IN NEW CALEDONIA

III. 1 Geological features

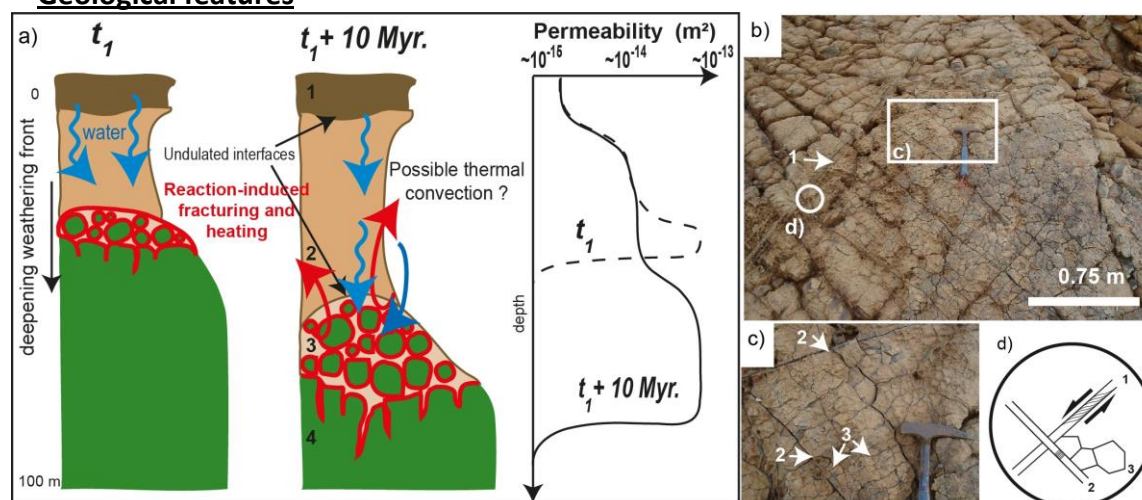


Figure 1 – a) Simplified lateritic profile upon ultramafic rocks of New Caledonia (NC), showing two distinct depth levels of the weathering front. Four main layers are distinguished: 1: ferricrete; 2: red mottled zone and fine yellow saprolite; 3: coarse saprolite; 4: unweathered peridotites. At left, physical conditions are insufficient to trigger thermal convection. Ten Myr later, reaction-induced fracturing and heating (shown by red contours) may trigger thermal convection. At right: qualitative temporal evolution of depth-dependent permeability; b) outcrop of dunites (Georges Pile, former mine southeast NC) showing three orders of fracturing; c) detail of outcrop b) showing second (2) and third (3) order fractures; d) relationships between fractures and displacement.

The peridotite massifs of New Caledonia's main island correspond to the remnants of a giant ophiolitic nappe, which was emplaced by obduction of the oceanic mantle during the Late Eocene. A large peridotite massif is present in the southeast of the island (30 km x 100 km) while several klippen (a few km wide and a few tens of km long) are exposed along the northwestern coast. The typical weathering profile consists of three main layers (Figure 1a): (i) a lower fractured coarse saprolite with an interconnected macroporosity ($\approx 0.2-0.4$) and a high hydraulic conductivity (1.7 to $4.3 \times 10^{-6} \text{ m s}^{-1}$, or, a permeability of ≈ 1 to $4 \times 10^{-13} \text{ m}^2$), (ii) a fine yellow saprolite (laterite stricto sensu.) and a red mottled zone with a high but poorly interconnected porosity ($\approx 0.5-0.7$) and lower hydraulic conductivity ($\approx 5 \times 10^{-7} \text{ m s}^{-1}$, or, a permeability of $\approx 5 \times 10^{-14} \text{ m}^2$), and (iii) an upper soft nodular ferruginous layer and/or a ferricrete, which caps the profile (Robineau et al., 2007; Traore et al., 2008).

The high permeability of the coarse saprolite layer can be linked to weathering-induced fracturing. Three kinds of fractures have been described in New Caledonia (Figure 1b-1d). The second and third order weathering-induced fractures (2 and 3 in Figures 1c-1d) show no displacement, but exhibit mechanical dilation signatures in all directions mostly due to olivine and pyroxene weathering.

III. 2 Field observations and borehole data

Undulations of the saprolite-bedrock interface (Figure 3) have been delineated from compilation of borehole data in numerous areas (e.g. Robineau et al., 2007). Recently, geological data from 298 boreholes in the Goro area have been collected and geo-statistically analyzed to build a better-defined 3D block model (Figures 3d to 3f). Undulations of bedrock topography clearly appear in this 3D model as the corrugated brown interface, evocative of “egg-box topography”. Without invoking lateral permeability contrasts (presence of fractured zones) or variations in degree of serpentinization, it is proposed below that occurrence of thermal convection may also create the observed bedrock topography.

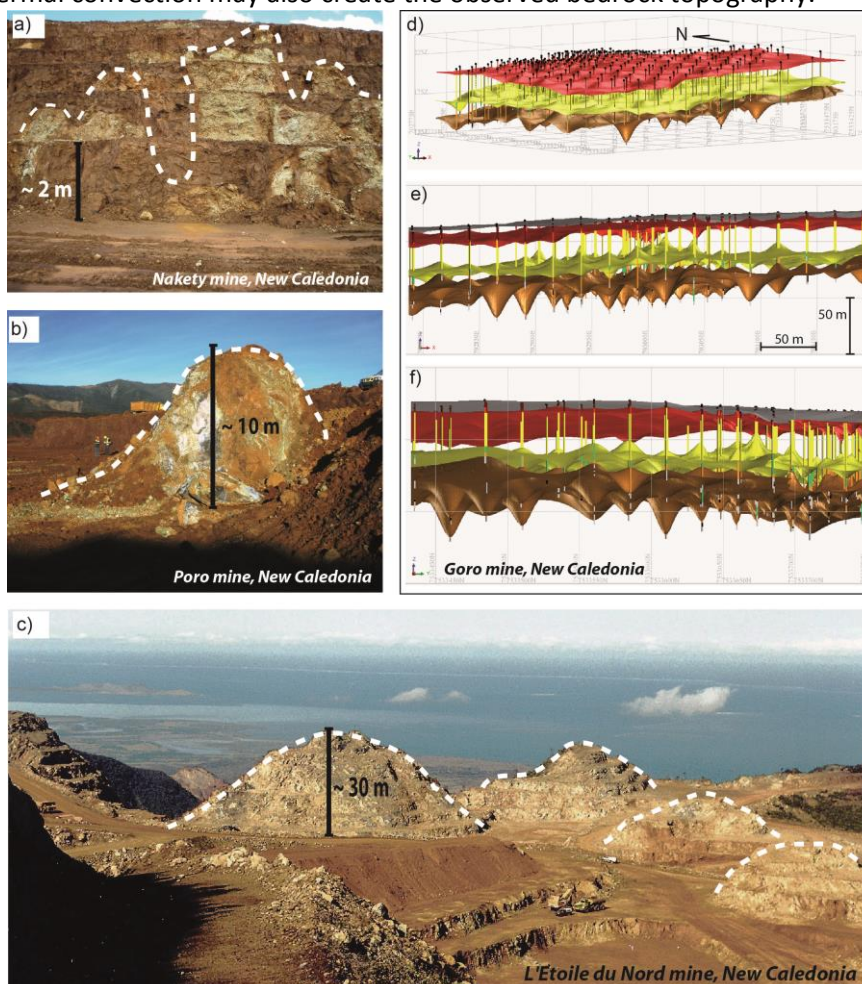


Figure 3 – Topographic undulations of saprolite-bedrock interface (white dashed line) from field observations (a-c) and borehole data (d-f). a) Small-scale undulations of the bedrock-saprolite interface; b) protrusion (or dome) of unweathered peridotite; c) large-scale and regularly spaced unweathered peridotite protrusions; d-f): 3D model of geological interfaces between the various units of the Goro laterite, as inferred from borehole data (vertical colored lines).

III. 3 Electric Resistivity Tomography

Previous Electrical Resistivity Tomography (ERT) investigations have improved our knowledge of the bedrock topography (Beauvais et al., 2007; Robineau et al., 2007). Topographic undulations of the saprolite-unweathered peridotite interface are evidenced at Tiébaghi. The bedrock topography apparently depends on surface topography: regular undulations are observed beneath a flat surface while an irregular topography of the weathering front is depicted under a sloping surface (see Beauvais et al., 2007).

Resistivity variations range from ≈ 0 to ≈ 120 Ohm.m. In fact, rock resistivity depends on porosity, pore structure, saturation, salinity and temperature (e.g. Hersir and Arnason, 2009). Thus, the lowest resistivity zones in ERT images could also correspond to the thermal imprint of hot fluids flowing (or having flown)

within the laterite. Although porosity and saturation play an important role in resistivity variations, it is worth viewing a thermal signature in ERT images.

III. 4 Likelihood of hydrothermal convection

In our geological context, high permeability values in the saprolite layers and anomalously high temperatures may trigger thermal convection, unless pressure-driven fluid flow dominates over buoyancy-driven flow. For a flat topography and a constant-thickness aquifer, thermal convection in a porous medium can occur as soon as the Rayleigh number exceeds the critical value of $4\pi^2$ (Lapwood, 1948):

$$Ra = \frac{g \alpha \Delta T k H}{\kappa \nu} > 4\pi^2 \quad (1)$$

where g is gravity (9.8 m.s^{-2}), α is the thermal expansion coefficient of water in $^{\circ}\text{C}^{-1}$, ΔT is the temperature contrast in $^{\circ}\text{C}$, k is the medium permeability in m^2 , H is the layer thickness in m , κ is the thermal diffusivity of water in $\text{m}^2 \text{ s}^{-1}$ and ν is the kinematic viscosity of water in $\text{m}^2 \text{ s}^{-1}$. When typical water properties at 20°C are used for a 100m -thick aquifer in which $\Delta T=60^{\circ}\text{C}$, then permeability greater than $\approx 3 \cdot 10^{-13} \text{ m}^2$ is needed to trigger convection. When different boundary conditions are considered, the critical Rayleigh number decreases to 3 (Phillips, 1991), and convection occur for permeability around 10^{-13} m^2 . If the physical properties are set at 50°C , then convection is triggered for permeability around $2 \times 10^{-14} \text{ m}^2$.

The present-day permeability values for the coarse saprolite of New Caledonia have been estimated at 1 to 4.3×10^{-13} (Join et al., 2005). These values being probably higher in the past, the physical conditions are very propitious for triggering convection. To proceed further in such investigations while accounting for realistic properties and representative geometries of laterites, a numerical approach is required.

IV. NUMERICAL MODELING

IV.1 Governing equations, fluid properties and “Rock Alteration Index”

Thermal convection within permeable media can be numerically studied by coupling heat transfer and fluid flow equations (Darcy law) with the appropriate physical properties (where fluid density and viscosity are temperature-dependent). These equations are identical as those described in Guillou-Frottier et al. (2013).

To describe mineralization patterns, Phillips (1991) introduced a simple parameter, called “Rock Alteration Index”, quantifying the rate of mineralization (or dissolution) of species present in the fluid. The rate of mineralization, Q_m , is directly proportional to the fluid velocity and to the temperature gradient:

$$Q_m \propto -RAI = -\vec{u} \cdot \vec{\nabla} T = -\left(u \frac{\partial T}{\partial x} + v \frac{\partial T}{\partial z} \right) \quad (2)$$

where u and v are the horizontal (x direction) and vertical (z direction) components of the fluid velocity. This index has been often used to describe mineralization patterns (e.g. Harcouët-Menou et al., 2009; Eldursi et al., 2009). The highest RAI is obtained when the fluid moves perpendicularly to the isotherms. Within zones of large negative values of RAI, the areas where fluid velocity is high, may be potentially mineralized by intense weathering, and can thus be defined by:

$$RAI = \vec{u} \cdot \vec{\nabla} T < 0 \quad \text{and} \quad U > 10^{-9} \text{ m.s}^{-1} \quad (3)$$

where U is the absolute value of the velocity. These areas are illustrated in red in Figures 6 and 7.

IV.2 Geometry, boundary conditions, and model for a deepening weathering front

The geometries of the preliminary and main models allow investigating the dynamic transition between topography-driven flow and buoyancy-driven flow (Figure 4). In the preliminary models (Figure 4a), the deepening of the weathering front was not considered, and a constant permeability was imposed through the saprolite layer. The basal temperature was set at 80°C . The topographic slope ranged from 0 to 10%. The medium permeability ranged from 10^{-15} to 10^{-12} m^2 . In the models of Figure 4b, the weathering front

deepens with local increase in heat production and permeability (Figure 4c). Fixed temperature conditions were imposed at the surface (20 °C) and at the base of the model (23 °C). An atmospheric pressure was also imposed at the surface, but there was no heat flow and no fluid flow across the other boundaries.

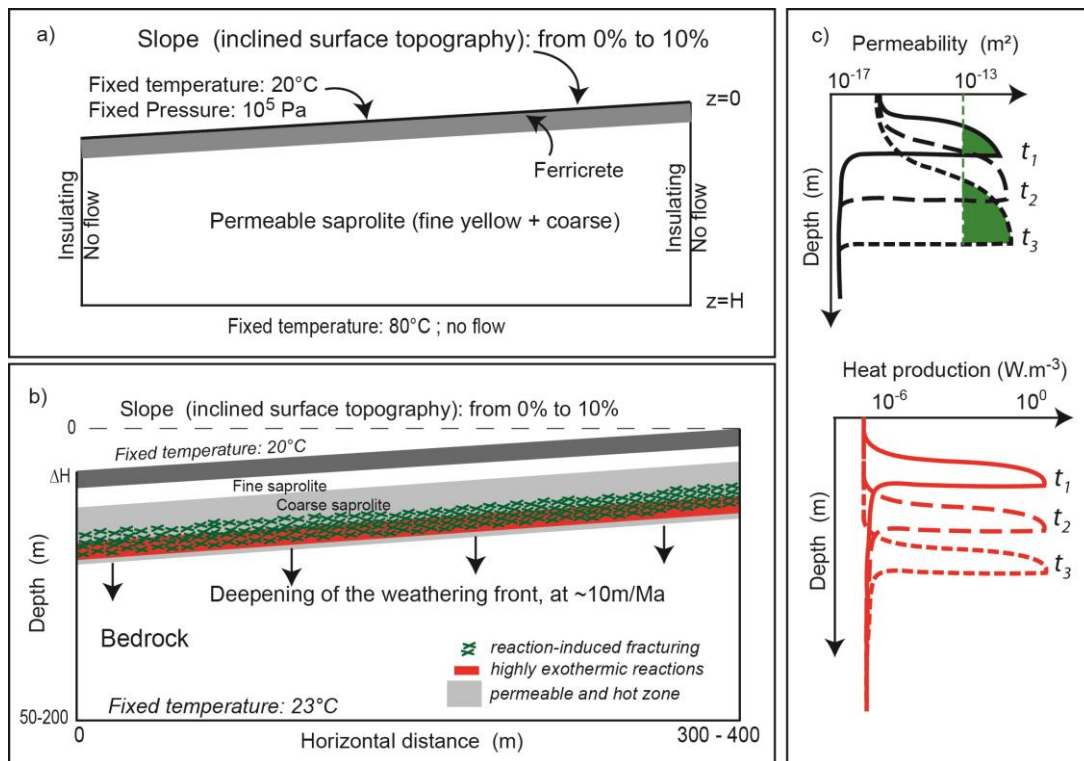


Figure 4 - a) Preliminary models with no deepening of the weathering front; b) Main models with a deepening front and varied surface slopes; c) the deepening of the weathering front (case b) induces time- and depth-dependent (permeability; heat production) values in the medium.

Exothermic reactions can be simulated at the weathering front by an equivalent heat production value so that high temperatures (several tens of °C) could be obtained after several million years of weathering. However, this value is unknown since (i) reaction kinetics depends on temperature and (ii) the number of reactions increases with time. Hydration of olivine is known to produce considerable heat (250 kJ kg⁻¹; McDonald and Fyfe, 1985), and the heat produced during the weathering of peridotites can be roughly estimated. Considering that a unit volume of peridotite 0.1 mm thick (the olivine grain size) times 1 m² contains 90 % of olivine, and assuming a weathering timescale of 40,000 years per meter (Trescases, 1975), then the equivalent 0.3 kg of peridotites (density being 3300 kg.m⁻³) will be weathered in 4 years, while producing 75 kJ. This is equivalent to a bulk heat production of 6.6 W.m⁻³. Given lower concentrations of olivine, or slower weathering velocity, the estimate falls to around 1 W.m⁻³. Hence, during numerical modeling, the local heat source will be adjusted to get temperatures around 60-80 °C near the weathering front, and a heat production value around 1W.m⁻³ is thus expected.

The vertical extent of exothermic reactions was simulated by using a semi-Gaussian type function (Figure 4c), whose half-width can be adjusted (a few meters for the “thermal thickness” of the weathering front, and a few tens of meters for its “permeable thickness”).

IV.3 Numerical procedure

Equations were solved with the Comsol Multiphysics™ software (finite element method), with which temperature- (and space-) dependent physical properties can be easily implemented (see benchmark experiments in Eldursi et al., 2009). During computation representing up to 25 Myr of water-rock interactions, the weathering front deepens with time. Fixed low permeability values of 10⁻¹⁵ m² are

imposed in the ferricrete layer and in the unweathered rocks. The initial thermal field consists of a linear temperature increase from the inclined surface (20 °C) to the bottom boundary. All other physical properties held constant in the simulations are: porosity (40%), permeability of unweathered rock (10^{-15} m²), density of solid (3300 kg.m⁻³), thermal conductivity of the fluid and the solid (0.6 and 3 W.m⁻¹.K⁻¹) and heat capacity of the fluid and the solid (4200 and 800 J.kg⁻¹.K⁻¹). Before describing how fluid flow regimes are established within such complex systems, results obtained from the preliminary models with homogeneous permeability beneath an inclined surface (Figure 4a) are first presented

V. RESULTS

V.1 Preliminary models

In the hydrogeologic model of the ultramafic massif of Tiébaghi (New Caledonia), Join et al. (2005) reproduced transmissivity and fluid flux data with Darcy velocity values ranging from 0.4 to 1.5×10^{-7} m s⁻¹. Preliminary models were performed in order to retrieve these velocity estimates.

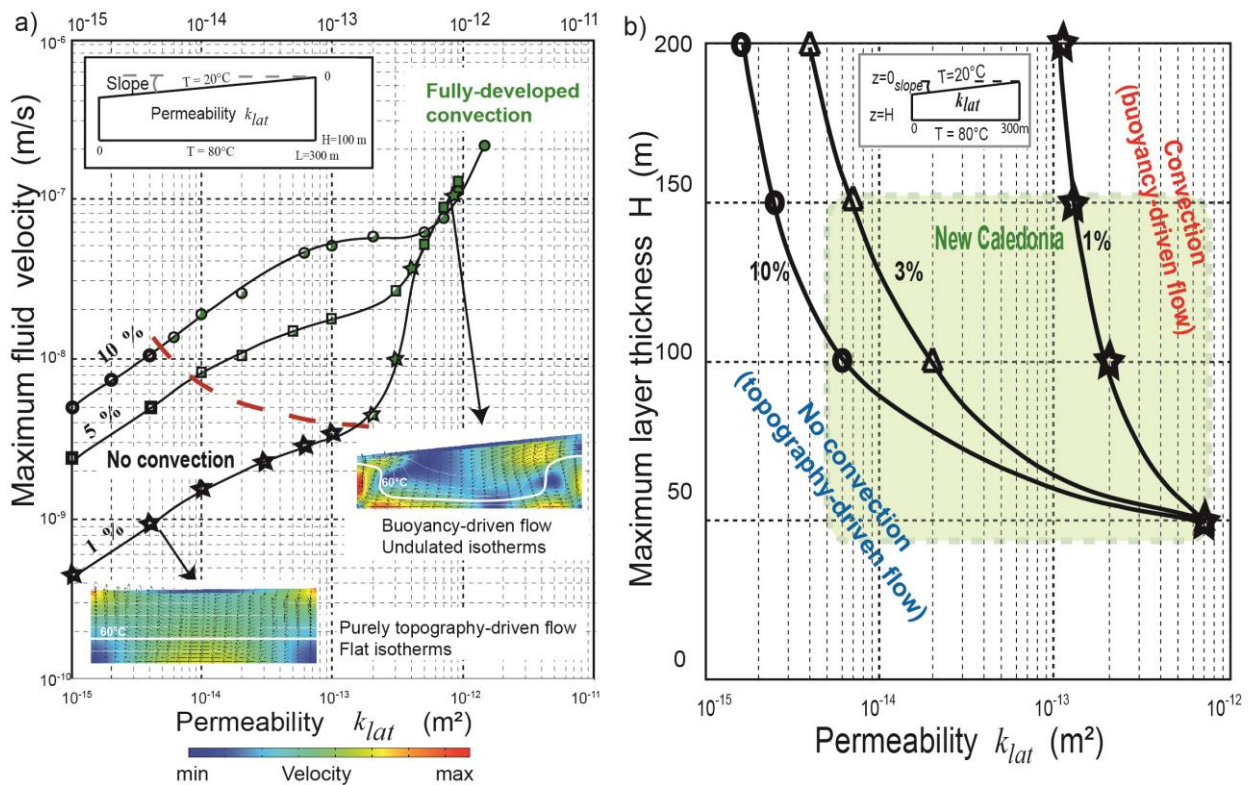


Figure 5 – Results of preliminary models where topographic slope, permeability, and layer thickness have been varied. a) Empty symbols (at left of the red dashed line) correspond to experiments with purely topography-driven flow, while green-filled symbols represent experiments where convection develops; b) regime diagram as a function of layer thickness, topographic slope and permeability.

As expected, the maximum fluid velocity increases with increasing permeability, regardless of the topographic slope (Figure 5a). For permeability lower than 4×10^{-13} m², the greater the topographic slope, the higher is the maximum fluid velocity. To reach the highest velocity estimate of 1.5×10^{-7} m s⁻¹, thermal convection is required (domain of green symbols in Figure 5a), regardless of the slope value. According to (1), thickness of the convective layer has also an effect on the convective regimes. In our case, the thickness of the permeable layer varies through time and space, and it is worth studying how it controls the convective regimes. The results are shown in Figure 5b. Note that the green area, showing parameter values for New Caledonia, includes both topography-driven and buoyancy-driven fluid flow regimes.

V.2 Models accounting for the deepening of the weathering front

Figure 6a illustrates two time steps of the temperature (colors and white contours) and velocity (arrows) fields for a typical experiment, using a topographic slope of 2.5 %, where the weathering front deepens at 2.5 m Myr^{-1} . When temperature at the weathering front exceeds $85 \text{ }^\circ\text{C}$, hydrothermal convection occurs as emphasized by undulations of the isotherms induced by vertical fluid motion. Figure 6b shows the areas where the RAI is negative and where fluid velocities are the highest. The less weathered zones (blue areas) exhibit a corrugated topography.

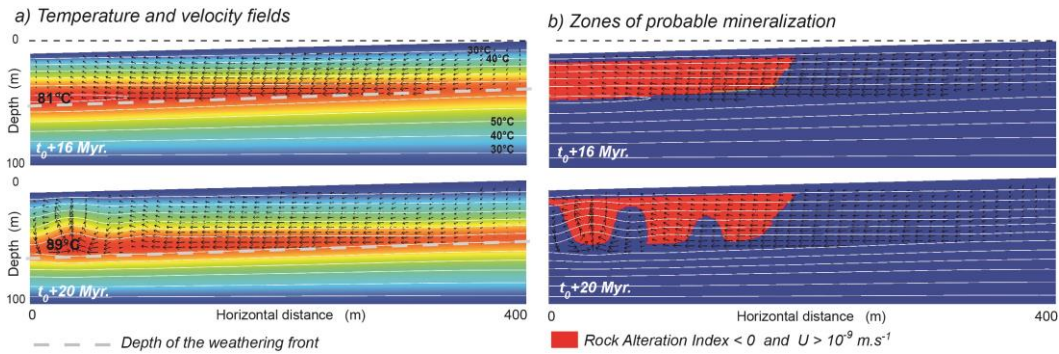


Figure 6 – a): hydrothermal convection with a maximum temperature of 89°C at the weathering front (grey dashed line). Maximum equivalent heat production: 0.8 W.m^{-3} ; maximum permeability: $7 \cdot 10^{-13} \text{ m}^2$. b): corresponding RAI patterns exhibiting a corrugated bedrock topography.

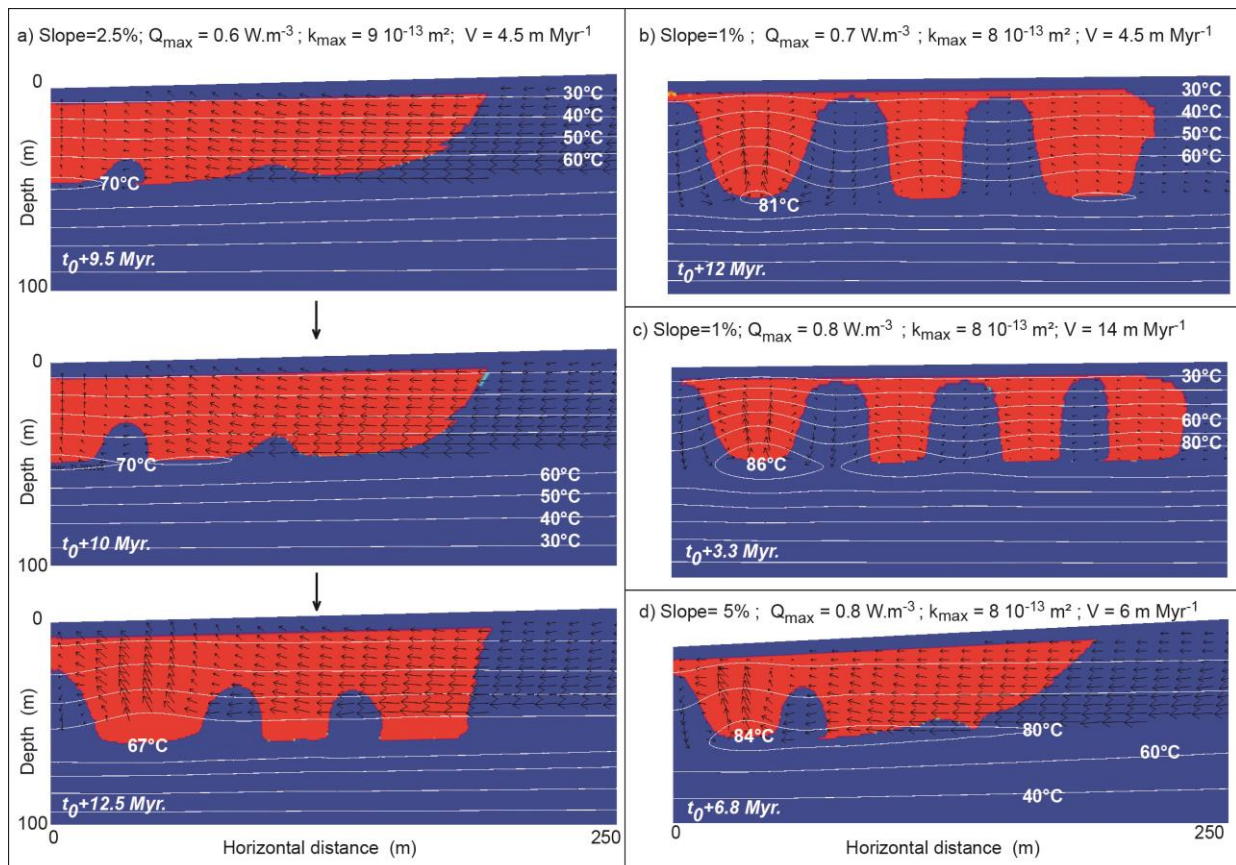


Figure 7– RAI patterns for different parameters, where front velocity (V) and topographic slope are varied. a) Temporal evolution showing spatially and temporarily varying undulations; b) and c) cases for a 1% topographic slope and different front velocities; d) case of a 5% slope.

It must be emphasized that hydrothermal convection is clearly less vigorous when the slope is important, because topography-driven flow is dominant. Figure 7 illustrates different RAI patterns where front velocity (“V”) and topographic slope are varied, and where maximum permeability (“ k_{max} ”) is slightly higher than present-day measurements, but probably representative of past permeability values.

The maximum equivalent heat production (Q_{max}) stays around 0.7 W.m^{-3} , yielding maximum temperatures below 87°C . Hydrothermal corrugations can also be obtained with maximum temperature values as low as 67°C for a permeability of $9 \cdot 10^{-13} \text{ m}^2$ (bottom plot of Figure 7a). Figures 7b to 7d show that wavelengths and amplitudes of corrugations are larger when topographic slope is small.

VI. CONCLUSION

Based on field observations, temperature data, images from electrical resistivity tomography, permeability and fluid velocity estimates, borehole and geological data inserted into a 3D geometrical model, we suggest that corrugated bedrock topographies can result from hydrothermal convection triggered by reaction-induced fracturing and heating. If the results obtained from the present two-dimensional numerical models were extrapolated to three dimensions, the undulations would probably form two-directional corrugations (“egg-box topography”) as suggested in Goro mine area (Figures 3).

Although we did not model a natural topographic profile that would include plateaus and/or slope changes, any attempt to reproduce field observations in greater detail should also account for additional effects, e.g. chemical and mechanical erosion, or tectonic and climatic forcing that may control hydrodynamics of weathering profiles and bedrock topography over the long term.

References:

- Amissé et al. (2010) - *RST2010, Bordeaux, France, 25-29 October*
Barnes I., O’Neil J.R., Trescases J.J. (1978) - *Geochem Cosmochim Acta*, 42, 144-145
Beauvais A., Parisot J.C., Savin C. (2007) - *Geomorphology*, 83, 1-13
Chavagnac V., et al. (2013) - *Geochem. Geophys. Geosys.*, 14, 7, 2474
Dewandel B., et al. (2005) - *Hydrogeol. J.*, 13, 708–726
Eldursi K., et al. (2009) - *Earth Planet. Sci. Lett.*, 288, 70-83.
Guillou-Frottier L., et al. (2013) - *J. Volcanol. Geotherm. Res.*, 256, 29-49
Harcouët-Menou et al. (2009) - *Geofluids*, 9, 116-137
Hersir G.P., Arnason K. (2009) - *Geothermal Training Program*, Santa Tecla, El Salvador, 17-30 October, 2009
Join, J.L., et al. (2005) - *C. R. Geosci.*, 1500-1508
Kelemen P.B., Hirth G. (2012) - *Earth Planet. Sci. Lett.*, 345-348, 81-89
Lachassagne P., Wyns R., Dewandel B. (2011) – *Terra Nova*, 23, 145-161
Lapwood E. (1948) - *Proc. Cambridge Philos. Soc.*, 44, 508–521
Launay J., Fontes J.C. (1985) - *Geol. Fr.*, 1, 83-100
McDonald A.H., Fyfe W.S. (1985) - *Tectonophysics*, 116, 123-135
Phillips O.M. (1991) – *Flow and reactions in permeable rocks*, Cambridge Univ. Press, New York, 285p.
Plümpner O., et al. (2012) - *Geology*, 40, 1103-1106
Quesnel B., et al. (2013) - *Geology*, 41, 1063-1066
Robineau B., et al. (2007) - *Austr. J. Earth Sci.*, 54, 773-781
Royne A., et al. (2008) - *Earth Planet. Sci. Lett.*, 275, 364-369
Traore D., et al. (2008) - *Amer. Mineral.*, 93, 22-30
Trescases J.J. (1975) - *Mémoires de l’ORSTOM*, 78, Paris, pp. 259
Vasconcelos P.M., Conroy M. (2003) - *Geochim. Cosmochim. Acta*, 67 (16), 2913-2930
Wenner D.B., Taylor Jr. H.P. (1971) - *Contrib. Min. Pet.*, 32, 165-185
Wyns R., et al. (2004) - *Bull. Soc. Géol. Fr.*, 175, 21-34